Prediction of permeability for porous media reconstructed using multiple-point statistics

Hiroshi Okabe[1,2] and Martin J. Blunt[1]
[1]*Department of Earth Science and Engineering, Imperial College London, SW7 2AZ, United Kingdom*
[2]*Japan Oil, Gas and Metals National Corporation, 1-2-2 Hamada, Mihama-ku, Chiba-shi, Chiba, 261-0025, Japan*
(Received 10 May 2004; published 23 December 2004)

To predict multiphase flow through geologically realistic porous media, it is necessary to have a three-dimensional (3D) representation of the pore space. We use multiple-point statistics based on two-dimensional (2D) thin sections as training images to generate geologically realistic 3D pore-space representations. Thin-section images can provide multiple-point statistics, which describe the statistical relation between multiple spatial locations and use the probability of occurrence of particular patterns. Assuming that the medium is isotropic, a 3D image can be generated that preserves typical patterns of the void space seen in the thin sections. The method is tested on Berea sandstone for which a 3D image from micro-CT (Computerized Tomography) scanning is available and shows that the use of multiple-point statistics allows the long-range connectivity of the structure to be preserved, in contrast to two-point statistics methods that tend to underestimate the connectivity. Furthermore, a high-resolution 2D thin-section image of a carbonate reservoir rock is used to reconstruct 3D structures by the proposed method. The permeabilities of the statistical images are computed using the lattice-Boltzmann method (LBM). The results are similar to the measured values, to the permeability directly computed on the micro-CT image for Berea and to predictions using analysis of the 2D images and the effective medium approximation.

DOI: 10.1103/PhysRevE.70.066135 PACS number(s): 02.50.Ey, 02.70.−c, 42.30.Wb, 83.80.Nb

I. INTRODUCTION

A. Reconstruction of porous media

The reconstruction of three-dimensional (3D) porous media is of great interest in a wide variety of fields, including earth science and engineering, biology, and medicine. The structural information obtained can be used to predict transport properties, using, for instance, pore-scale network modeling models [1] or lattice Boltzmann simulation [2].

A variety of methods have been used to create 3D pore space images including serial sectioning [3], focused ion beam [4,5], laser scanning confocal microscopy [6], and x-ray computed tomography [7,8]. Figure 1 shows a micro x-ray CT image of Berea sandstone imaged at a resolution of approximately 10 μm [9]. In addition, the porous medium can be reconstructed by modeling the geological processes by which it was formed [10–12].

However, in many cases the submicron structures present in many rocks, particularly carbonates [13], preclude direct imaging, and the geological history is too complex for process-based reconstruction to be applied easily. In these cases, it is necessary to construct 3D structures from more readily available two-dimensional (2D) images.

B. Stochastic reconstruction

Two-dimensional thin sections are, in contrast to 3D images, often readily available at high resolution. Geometrical properties, such as the porosity and the two-point correlation function, can be measured from these sections and used to generate a 3D image with the same statistical properties. This has the advantage of being quite general, allowing a wide variety of porous media to be described. Reconstruction of a 3D binary image given the porosity and two-point autocorrelation function of a 2D thin section has been widely applied [14,15]. However, these two constraints have been found to be insufficient to reproduce the microstructure of particulate media, such as grain or sphere packs [9,16]. The simulated annealing method is a popular reconstruction method, which can improve the results through the use of additional morphological descriptors, such as lineal path function, pore and solid phase chord distributions [17–19]. Recently a sort of pattern recognition approach using a small template has been developed [20]. This is an efficient method

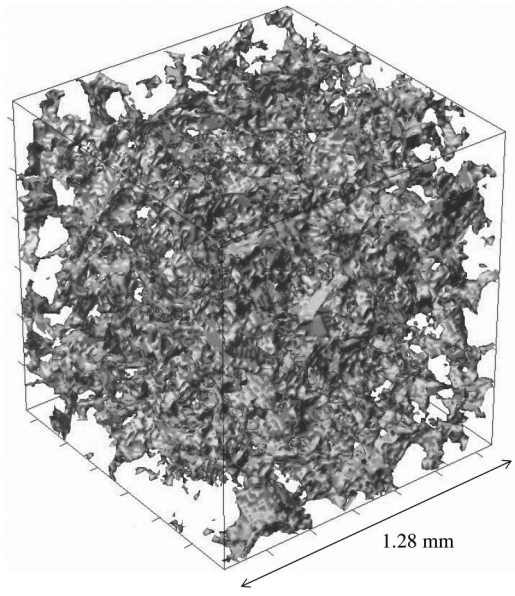

FIG. 1. A 3D pore-space image of Berea sandstone. The pore space is shown in gray. The image was generated using micro-CT scanning with a resolution of approximately 10 μm [9].

for generating a wide variety of pore structures in 2D by replicating patterns in a five-point stencil using a Markov chain Monte Carlo methodology. Our multiple-point statistics approach, described later, is a generalization of this technique, where we capture patterns described in a template of arbitrary size to capture large-scale patterns in the pore space. The use of multiple-point statistics is more general than the three- and four-point statistical correlation functions used by Yao *et al.* [21]. As we discuss below, the disadvantage of ignoring multiple-point statistics is that the simulated pore space may ignore the long-range connectivity of the pore space [22–24]. For example, Manwart *et al.* [23] provided a detailed investigation of their method [17,18] through computation of the local porosity and showed that incorporation of only the autocorrelation function and the lineal path function in the reconstruction method may show significant differences of the geometrical connectivity between the reconstructed and the experimental samples.

C. Multiple-point statistics

We will pursue the multiple-point statistical technique introduced in geostatistics to represent connected geological bodies, such as sand channels, at the field scale [25]. Our problem is conceptually similar—we need to generate pore spaces that have a high degree of interconnectivity. In previous work [26], we have applied this methodology to study the percolation probabilities of Berea and Fontainebleau sandstones that have already been characterized by other means [27,28]. In this paper, for completeness, we first describe the technique and then apply it to study both sandstone and carbonate samples. The long-range connectivity of the pore structure is tested by measuring the percolation probability and by predicting permeability using the lattice-Boltzmann method. In addition permeabilities of the structures are predicted directly from 2D images using the effective medium approximation.

II. RECONSTRUCTION OF PORE-SPACE REPRESENTATIONS

A. Need for higher-order information

Recent studies have cast doubt concerning the ability of traditional spatial correlation functions to describe rock texture, especially in terms of the reproduction of the connectivity of the media [22,27]. Traditional stochastic reconstructions using Gaussian random fields and simulated annealing are limited to the reproduction of low-order statistics inferred from readily available 2D images. Identification of low-order statistics is, however, not sufficient to reproduce connected long-range geometry or patterns with characteristic shapes (e.g., pore spaces) for some cases, such as media with low porosity. The reconstruction of such specific patterns calls for the characterization of the spatial continuity at three or more locations at a time. Reproduction of multiple-point continuity in the structure is critical, not so much to produce geologically realistic images, but also to provide accurate flow predictions through the structures. A more realistic reconstruction can be obtained by using structural information beyond the two-point correlation. A straightforward way to reproduce a geologically realistic structure with specific shapes consists of generating patterns with shapes observed in a reference and then distributing these patterns over the model.

Strebelle *et al.* [25] pioneered an approach that combines the easy conditioning of pixel-based algorithms with the ability to reproduce patterns of object-based techniques. The complex geological structures expected to be present at the field scale are characterized by multiple-point statistics. Such multiple-point statistics can be read from training images. The multiple-point statistics inferred from the training images are then exported to the model, where they are anchored to the conditioning data using a pixel-based sequential simulation algorithm. Their algorithm was used to simulate a turbidite reservoir where flow is controlled by meandering channels. The final numerical models reproduced these channel patterns and honored all conditioning data. Caers [29] applied this method to a synthetic sand channel reservoir. He compared the realization generated by the multiple-point method with a traditional indicator method [30] using the exhaustive variogram of the training image as a model. The use of two-point statistics failed to reproduce the channeling behavior. The multiple-point method, which appeared to be practical, general, and fast, can be applied to our problem at the pore scale.

We will make one major extension of the method. In the work of Strebelle *et al.* [25] and Caers [29], 2D training images were used to generate 2D statistical realizations. In this paper we will generate 3D images from 2D images.

B. Multiple-point statistics method

The extraction of multiple-point statistics from the training image and their reproduction in a stochastic model mainly consists of two steps: (i) extracting multiple-point statistics from training images and (ii) pattern reproduction.

The training image in Fig. 2 is scanned using a template t composed of n_t locations $\vec{u}_\alpha$ and a central location $\vec{u}$

$$\vec{u}_\alpha = \vec{u} + \vec{h}_\alpha \quad \alpha = 1, \ldots, n_t, \tag{1}$$

where the $\vec{h}_\alpha$ are the vectors describing the template. For instance, in Fig. 3(a), $\vec{h}_\alpha$ are the 80 vectors of the square 9 $\times$ 9 template.

The training image is scanned by the template in order to collect the pattern (P) at each location $\vec{u}$. The pattern, for instance shown in Fig. 3(b), is defined by

$$p(u) = \{i(\vec{u}); i(\vec{u} + \vec{h}_\alpha), \alpha = 1, \ldots, n_t\} \tag{2}$$

where $i(\vec{u})$ is the data value at the point within the template. Each point in the template has a number to identify the pattern and to store the pattern in memory. The set of all patterns scanned from the training image results in a *training data set*

$$Set = \{p(u_j), j = 1, \ldots, N_t\}, \tag{3}$$

where *Set* refers to the training data set constructed with the template t. N_t is the number of different central locations of template t over the training image.

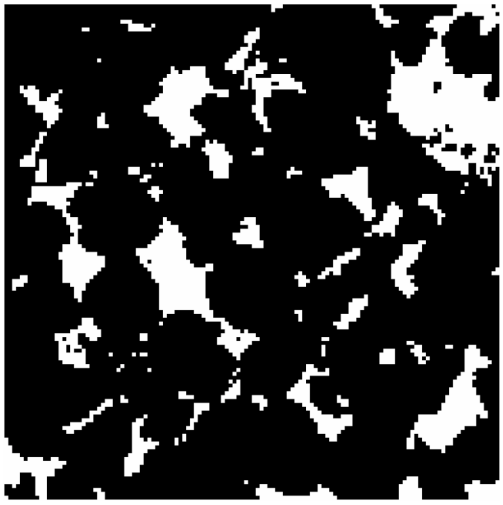

FIG. 2. Thin section used as a training image for Berea sandstone with a porosity of 0.1773 (128^2 pixels). The pore space is shown white and the grain black. The resolution of the image is 10 μm.

We use binary thin section images that have only void or solid. A detailed discussion of the training image can be found in Sec. IV.

Multiple-point statistics are probabilities of the occurrence of patterns. The probability of occurrence of any pattern p_n can be inferred from the training image by counting the number $c(p_n)$ of replicates of p_n, which should have the same geometry and the same data values. Then the multiple-point statistics can be identified to the proportion

$$\Pr(p_n) \approx c(p_n)/N_n, \tag{4}$$

where N_n is the size of the training image. The key is the determination of the local conditional probability distribution functions (CPDF). We need to evaluate the probability that the unknown attribute value $i(\vec{u})$ takes any of two possible phases—void or solid—given n nearest data during the reproduction at any unsampled location $\vec{u}$. If multiple-point statistics are available, then the conditioning of $i(\vec{u})$ to the single global pattern p_n can be considered, and the conditional probability can be identified to the training proportion.

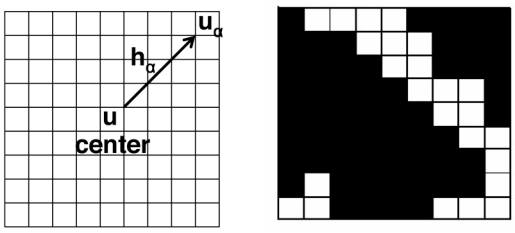

(a) (b)

FIG. 3. (a) A 9×9 template to capture multiple-point statistics. The training image is scanned and each occurrence of any possible pattern of void space and solid is recorded. (b) A pattern measured by a 9×9 template. The frequency of every possible pattern is found by scanning the template over the training image.

The CPDF is inferred directly and consistently from the training image.

To generate a 3D structure from 2D information, measured multiple-point statistics on one plane are rotated 90° around each principal axis. Measured statistics on the *XY* plane are transformed to the *YZ* and the *XZ* planes with an assumption of isotropy in orthogonal directions. At every voxel (volume pixel) in order to assign void or solid phase, three principal orthogonal planes *XY*, *XZ*, and *YZ* intersecting this voxel are used to find conditioning data on these planes one by one. Each probability of the phase at this voxel on the different planes is estimated by this process. To obtain a single probability on this voxel, the weighted average by the number of conditioning data on each plane is used to combine three probabilities. Finally, the phase at the voxel is assigned based on this combined probability to generate a 3D image. There is less conditioning data during the initial stage of the reproduction when sufficient conditioning data are not available. In this case, the porosity value can be used as the probability. Simple weighted probabilities are used for our pore-scale reconstruction; however, another method to combine different probabilities has been developed [31]. This formula combines different probabilities based on the different conditioning data and will introduce formal data interdependence. In this work, though, this method was not tested.

Finding and storing all required CPDF from a training image easily results in the acquisition of excessive amounts of information. Inference of a probability distribution function conditional to a pattern requires sufficient occurrences, which are dependent on the size of the training image, should be found. For our reconstruction, each of the 80 nodes in the data template (9×9 square shape) except a center point can take two phases (void or solid). The total number of possible patterns is thus 2^{80}, which means that only a relatively small number of CPDF can be actually inferred from the training image. To remove this problem, at each unsampled node, we infer the local CPDF by scanning the training image with progressive reduction of the size n of the conditioning pattern p_n until a designated minimum number of replicates of p_n are found. To minimize the repetitive process and the CPU time, each unsampled grid node is visited only once using a random path and each simulated value becomes a conditioning datum value. Conditioning data are frozen at their data location and used for the successive simulation. These cycles are iterated until all the voxels points are simulated. In order to avoid the repetitive scanning of the training image and to store multiple-point statistics effectively, a dynamic data structure called a search tree is used to store all training CPDF in advance. The algorithm is explained by a flow chart in Fig. 4.

A large template is necessary to reproduce large-scale structures. The template size can be theoretically expanded to match the largest structure in the training image. However, the template size is limited by memory limitations in the numerical simulation. This problem is solved using a variety of multigrid simulation [25,29]. Four different sized templates are used to scan the training image, resulting in four different data sets *Set* t_1, *Set* t_2, *Set* t_3, and *Set* t_4. Larger scale templates can simply be expanded from the small-scale template. In a multigrid system, a simulation is first per-

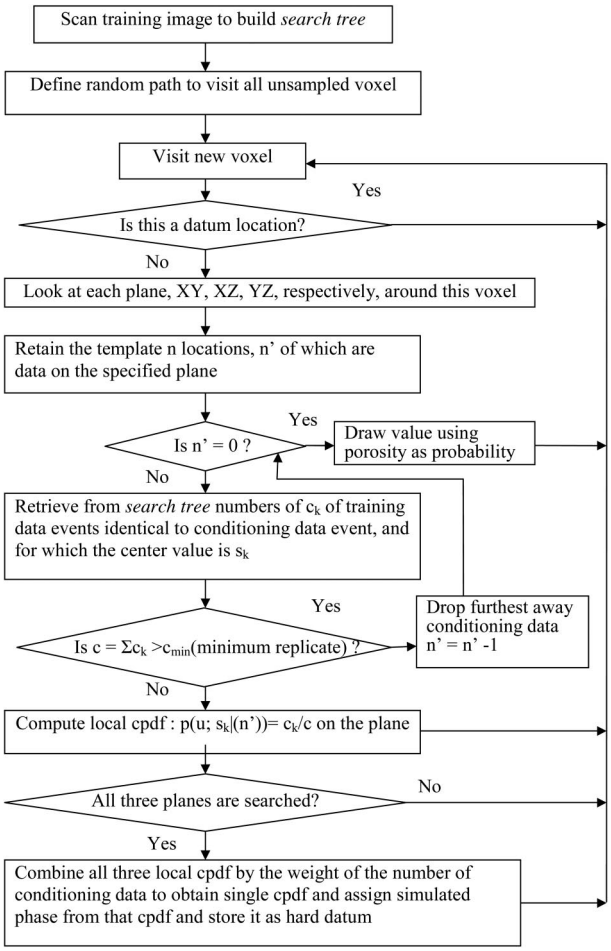

FIG. 4. Flow diagram of multiple-point statistics reconstruction of pore space images.

formed on the coarsest grid. Once the coarse simulation is finished, the simulated values are assigned to the correct grid locations on the finer grid and used as conditioning data on the finer grid. When large-scale structures exist in the training image, this multigrid approach captures the large-scale multiple-point statistics effectively while requiring relatively little memory.

C. Image processing

Unrealistic noise in the image due to insufficient statistics can be reduced by image processing. Nonpercolating regions of the solid phase correspond to islands isolated inside the void phase. Since this is impossible in real porous media, they were changed to appear as void phase. This process may slightly increase the porosity of the reconstructed structure; however, we confirmed the effect of changing structure was negligible by comparing the two-point correlation function in the reference and the reconstruction. In addition to this process, we use simple binary image processing to reduce noise in the void phase and smooth the boundary between void and solid. First we use a 3D opening operation in a 3^3 cubic neighborhood pattern containing a total of 27 pixels [32]. We have confirmed this simple operation reasonably smoothes the 3D image and reduces the noise. The image has a different porosity from the original after opening operation. We adjust the porosity by counting the number of neighbor pixels of the other phase in a 3^3 region and compare this number to some threshold value (coefficient value). The phase of the central pixel is changed if the count is exceeded. The coefficient value is chosen to result in the correct, original, value of porosity.

III. NUMERICAL METHODS

A. Effective medium approximation (EMA)

If the 3D microstructure is available, then solving the Navier-Stokes equations by, for instance, the lattice-Boltzmann method can yield the permeability with reasonable accuracy at the expense of extensive data collection and computation. On the other hand, a quick estimation of permeability directly from a 2D image can be made by the extended version of the EMA [33]. First the pore size distribution is estimated from the 2D image. The perimeter P and area A of each pore in a 2D image are estimated by the image analysis in order to approximate the hydraulic radius $C_i = A^3/P^2$. A stereological correction multiplies the hydraulic radius to obtain a more realistic conductance. The EMA replaces each conductance C_i in a pore network with the effective value C_{eff}. The effective conductance can be found by solving the following equation:

$$\sum_{i=1}^{N} \frac{C_{eff} - C_i}{(z/2-1)C_{eff} + C_i} = 0, \tag{5}$$

where z is the coordination number that represents the number of throats connected to each pore. Assuming a cubic network ($z=6$), the permeability is calculated using

$$k = \frac{NC_{eff}}{1.47A_{total}}, \tag{6}$$

where N is the number of conductors in the designated direction and A_{total} is total area. The number density correction factor, which is derived for the number density of pore intersections made by an arbitrary slice in a cubic network, is 1.47. More details can be found in Lock *et al.* [33].

B. Lattice-Boltzmann method (LBM)

The lattice-Boltzmann method (LBM) provides a good approximation to solutions of the Navier-Stokes equations using a parallel and efficient algorithm that readily accommodates complex boundaries, as encountered in porous media [34,35].

1. Model description: 3D single-phase model

Japan Oil, Gas and Metals National Corporation (JOGMEC, the successor to Japan National Oil Corporation) has developed a 3D two-phase LB model based on the 2D two-phase LB model proposed by Grunau *et al.* [36]. The model has been validated by precise comparisons with empirical equations, analytical solutions, and experiments [37]. We use

this LBM as a single-phase flow simulator in this study. The model for the single phase can be described as

$$f_i(\mathbf{x}+\mathbf{e}_i,t+1)-f_i(\mathbf{x},t)=\Omega_i(f_i(\mathbf{x},t)), \tag{7}$$

where $f_i(\mathbf{x},t)$ is the particle distribution function at space $\mathbf{x}$ and time t along the ith direction ($i=0,1,2,\ldots,18$ in our case). $\Omega_i(f_i(\mathbf{x},t))$ is the collision operator and $\mathbf{e}_i$ is the local particle velocity. We use a three-dimensional 19-velocity model, D3Q19. D3Q19 has 19 velocity vectors including a rest vector.

The collision operator $\Omega_i^{(BGK)}$ represents the relaxation process to local equilibrium as well as 2D LBM. We use the Bhatnagar-Gross-Krook (BGK) [38] collision operator. This operator is widely used due to its simplicity,

$$\Omega_i^{(BGK)}=-\frac{1}{\tau}[f_i(\mathbf{x},t)-f_i^{(eq)}(\mathbf{x},t)], \tag{8}$$

where τ is the single time-relaxation parameter and $f_i^{(eq)}$ is the local equilibrium state depending on the local density and velocity. The local equilibrium state can be chosen with the conservation of mass and momentum. Our local equilibrium distribution functions in the D3Q19 model are described below, depending on the direction:

$$f_0^{(eq)}=\rho\left(\tfrac{1}{3}-\tfrac{1}{3}u^2\right), \quad i=0 \quad \text{(for the rest position)}$$

$$f_1^{(eq)}=\rho\left[\tfrac{1}{18}+\tfrac{1}{6}(\mathbf{e}_i\cdot\mathbf{u})+\tfrac{1}{4}(\mathbf{e}_i\cdot\mathbf{u})^2-\tfrac{1}{12}u^2\right],$$

$$i=1,\cdots 6 \text{ (for rectangular directions)}$$

$$f_2^{(eq)}=\frac{\rho}{2}\left[\tfrac{1}{18}+\tfrac{1}{6}(\mathbf{e}_i\cdot\mathbf{u})+\tfrac{1}{4}(\mathbf{e}_i\cdot\mathbf{u})^2-\tfrac{1}{12}u^2\right],$$

$$i=7,\cdots 18 \text{ (for diagonal directions)}, \tag{9}$$

where ρ and u are the density and the local velocity, respectively. Thus, 3D single-phase LBM can be described as follows:

$$f_i(\mathbf{x}+\mathbf{e}_i,t+1)-f_i(\mathbf{x},t)=-\frac{1}{\tau}[f_i(\mathbf{x},t)-f_i^{(eq)}(\mathbf{x},t)]. \tag{10}$$

2. Boundary conditions

The bounce-back scheme at walls [39] is used to obtain no-slip velocity conditions. By the bounce-back scheme, when a particle distribution moves to a wall, the particle distribution scatters back to the node it came from. This simple boundary scheme allows the LBM to simulate fluid flows in complicated geometries. The flow field is computed using periodic boundary conditions.

3. Finite-size effects

There are finite-size effects and a kinetic-viscosity (or relaxation parameter) dependency in the LBM [40,41] (Fig. 5). Simulations with a finer discretization yield lower permeabilities. The predicted permeability also decreases with a decrease in the kinetic viscosity $\nu=(2\tau-1)/6$. Smaller values of ν generally decrease the finite-size effects. Deciding on appropriate values for ν (or τ) and the discretization level is still an open question and is not yet fully understood. For our results we take the pixel size of the images as the lattice spacing (10 μm for Berea sandstone and 0.345 μm for the carbonate rock) and $\tau=0.6$ for both cases. Although the models with different lattice spacing and τ yield different permeabilities, keeping the parameters fixed, especially for Berea sandstone, allows a fair comparison of the permeability on the images reconstructed using micro-CT scanning and multiple-point statistics.

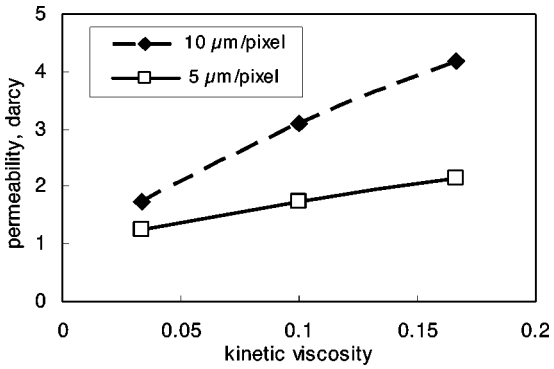

FIG. 5. Finite-size effects and the kinetic-viscosity effect in the LBM using Berea sandstone. A subgrid of the micro-CT image (size 64^3, porosity=0.1745) is taken and its size is doubled to confirm the effects of lattice spacing on the predicted permeability.

IV. ROCK SAMPLES

A. Berea sandstone

The x-ray microtomographic image of Berea sandstone is used as the experimental reference data and parts of the training image for our reconstruction method. The sample has a porosity of 0.1778 compared to 0.23 of the larger original core, which has a permeability of 1.1 D [9]. The differences between the porosity of the original core and that of the microtomographic data are due to the heterogeneity of the sandstone, the difference in sample size, and the resolution of the microtomography. The experimental sample is referred to as micro-CT in the following. 2D slices of the micro-CT images are shown in Fig. 2.

B. Carbonate rock

The carbonate rock sample used in our study consists of limestone and is classified as bioclastic packstone/grainstone. The core plug of this rock with 38 mm diameter and 70 mm long has a porosity of 0.318 and a permeability of 6.7 mD. A conventional CT measurement with a lower resolution than micro-CT reveals that the porosities in the measured voxels vary from 0.25 to 0.40 for the plug [42]. As described before, there is no 3D microstructure for this rock because the mean pore size is smaller than the resolution of micro-CT scanning. A backscattered electron micrograph image shown in

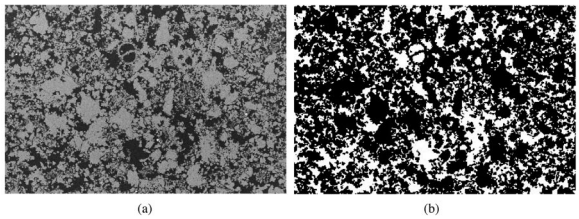

FIG. 6. (a) Backscattered electron micrograph image of the carbonate rock. (b) The image after binarization for the permeability estimation (1536×1024 pixels, the average porosity $= 0.357$).

Fig. 6 is used as a training image in order to reconstruct a 3D structure by our method.

C. Selection of a 2D thin section

Porosity measured from a 2D slice of a micro-CT image of the sandstone fluctuates as shown in Fig. 7. In order to reconstruct a 3D structure effectively from 2D cuts, a representative 2D image should be selected especially in terms of porosity. We take the slice indicated in this figure by an arrow that has a porosity close to that of the whole sample.

For the carbonate rock, a part of the binarized thin-section image is used as the training image. A 512×512 pixel image with a porosity of 0.331 shown in Fig. 8 is selected from the original larger image [Fig. 6(b)] to reduce the computation time in the reconstruction process.

V. RESULTS

A. Permeability estimation by EMA

The permeability of each sample is estimated directly from the 2D images. A stereological correction factor of 0.44 is multiplied to the measured hydraulic radius [33]. Assuming a cubic network, the coordination number of six is used in our estimations. We know the assumption of cubic pore network might be oversimplified; however, the EMA is useful to estimate permeability without massive computational requirements and to evaluate a 2D image in advance of 3D reconstruction. Estimations of permeabilities for both Berea sandstone and the carbonate rock are in reasonably good agreement with experiment data as shown in Table I, although the size of the samples is different.

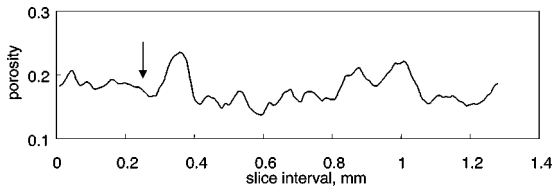

FIG. 7. Porosity fluctuation within a measured microstructure of Berea sandstone. The average porosity is 0.1775, slice size $= 1.28 \times 1.28$ mm^2, slice interval $= 10.0$ μm. The arrow indicates the slice, from which our training image was taken, which has a porosity close to the average.

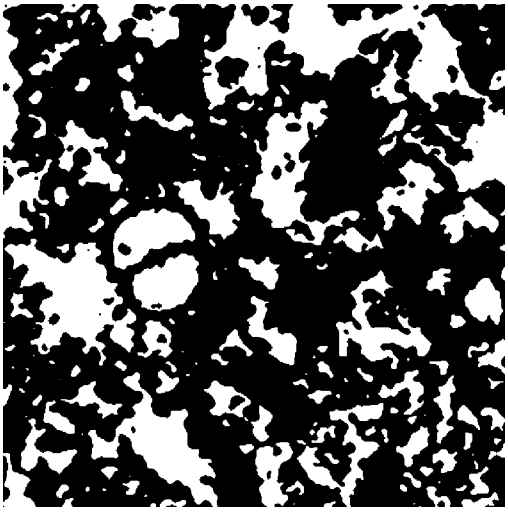

FIG. 8. A selected binary image of the carbonate rock. The image size is 512×512 pixels (0.345 μm/pixel) with a porosity of 0.331.

B. Template selection

We use four different sized templates with the same 9×9 square shape, spanning 9×9, 18×18, 36×36 and 72×72 pixels. A larger template is preferable in order to capture large structures directly; however, it takes much more CPU time and introduces more noise if the training image does not provide sufficient statistics. For example, if the square templates were expanded from 9×9 to 11×11 with same four-stage multigrid system, the CPU time approximately doubled for a 150^3 structure. A smaller template leads to a reconstruction with fewer constraints and less noise, but large structures are not so accurately reproduced. We decided to use a 9×9 template after considering larger and smaller templates—this gave the optimum combination of CPU time, lack of noise, and preservation of large features in the pore space.

C. Unconditional 3D reconstruction

A 3D subgrid of reconstructed Berea sandstone is visually compared with that of micro-CT image in Fig. 9. In order to suppress unrealistic noise and smooth the image, postprocessing (opening operation) is used as described before. Then additional erosion is applied in order to adjust the porosity values. The noise is significantly reduced and characteristic structures of the void space are reasonably preserved after the processing. The porosity of each 2D slice is de-

TABLE I. Estimated permeability mD. Note that in the LBM column, (CT) indicates the predicted permeability computed directly on the micro-CT image. Other values indicated (Re) are calculated on the reconstructed structures.

	Experiment	EMA	LBM
Berea	1100	1448	(CT) 1346, (Re) 1274
Carbonate	6.7	6.05	(Re) 19.8

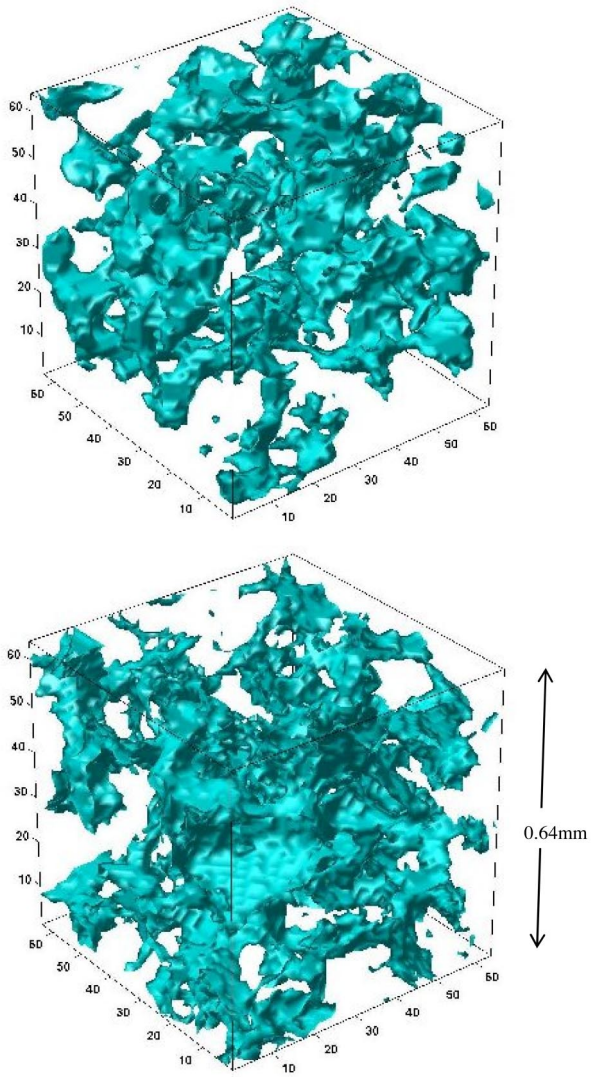

FIG. 9. A 3D subgrid of reconstructed Berea sandstone (above, $\phi=0.1747$) compared to that of the micro-CT image (below, $\phi=0.1781$).

creased or increased slightly from the original image; however, it is not drastically changed and the porosity in 3D is preserved. The reconstructed image in Fig. 9 is well reproduced. The smaller reconstructed image of the carbonate rock is also shown in Fig. 10. However, it is difficult to judge this image because there is no 3D reference microstructure. The 2D cuts of the 3D reconstruction of the carbonate rock without conditioning data are shown in Fig. 11.

D. Conditional 3D reconstruction

In order to generate a more realistic structure, a part of the training image can be used as conditioning data. This is not always necessary for this case because the amount of conditioning data from the training image is limited. The constraints, however, affect the reconstruction in the region near the conditioning data. Figure 12 shows 2D cuts of a conditional 3D multiple-point reconstruction after postprocessing.

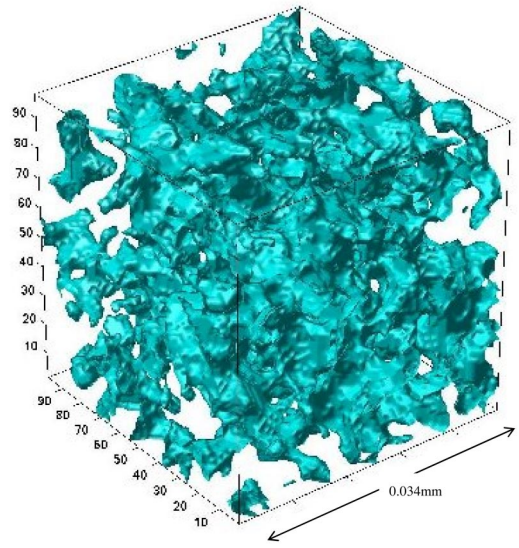

FIG. 10. A 3D subgrid of reconstructed carbonate rock ($\phi=0.318$).

The reconstruction of the carbonate rock with 150^3 voxels took approximately 14 h CPU time with an Intel Xeon 1.7 GHz computer. A part of the 2D training image is used as conditioning data. In Fig. 12, the quality of the image is better near the conditioning data and typical pore shapes are more poorly reproduced away from the conditioning plane or in orthogonal directions. We assume that the structures are isotropic. For anisotropic media it should be possible to incorporate information from several training images taken in orthogonal directions.

E. Autocorrelation function and specific surface area

Traditional two-point statistical reconstruction uses the void-void autocorrelation function of the 3D microstructure as one of the matching parameters. When the microstructure is defined by the binary phase function [$Z(r)=1$ if r belongs to void space, $Z(r)=0$ otherwise], the void-void autocorrelation function $R_Z(u)$ is defined by

$$\phi=\overline{Z(\vec{r})} \tag{11}$$

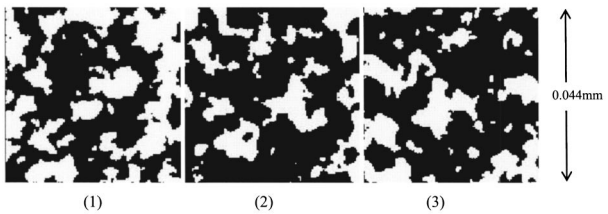

FIG. 11. The 2D cuts through an unconditional 3D reconstruction of the carbonate rock (128^3, 0.345 μm/pixel) with the slice porosities ϕ indicated. The images are postprocessed. (1) XY plane ($Z=64, \phi=0.4245$), (2) XZ plane ($Y=64, \phi=0.2844$), (3) YZ plane ($X=64, \phi=0.2964$).

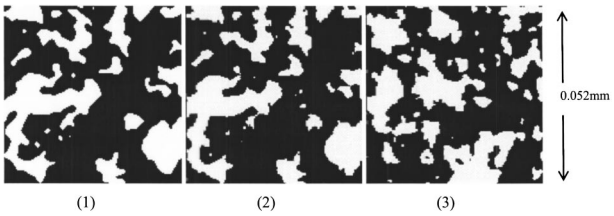

FIG. 12. The 2D cuts through a conditional 3D reconstruction of the carbonate rock (150^3, 0.345 μm/pixel) with the slice porosities ϕ indicated. The images are postprocessed. (1) *XY* plane ($Z=75$, conditioning data, $\phi=0.3202$). (2) *XY* nearest conditioning plane ($Z=74$, $\phi=0.3167$). (3) *XZ* plane ($Y=75$, $\phi=0.3433$).

$$R_Z(u) = \frac{\overline{[Z(\vec{r}) - \phi][Z(\vec{r}+\vec{u}) - \phi]}}{[\phi - \phi^2]}, \tag{12}$$

where overbars denote statistical averages and u is a lag vector.

The autocorrelation function of our Berea sandstone is virtually identical in the coordinate three directions confirming that the structure is isotropic [26]. Figure 13 shows the autocorrelation functions of the reconstructed Berea sandstone averaged over three orthogonal directions compared to those measured on the micro-CT image and on the 2D training image. The agreement is excellent, demonstrating that the multiple-point statistics method reproduces two-point statistics accurately.

F. Fraction of percolating cells in the reconstructed microstructure

Visual inspection of structures does not reveal the degree of connectivity of the structure. Porosity, specific surface area, and two-point correlation functions are also insufficient to distinguish different microstructures because they are all low-order information. A quantitative characterization of the connectivity is provided by the local percolation probabilities or fraction of percolating cells [43] defined by

$$p_3(L) = \frac{1}{m}\sum_r \Lambda_3(r,L), \tag{13}$$

where m is the number of measurement and $\Lambda_3(r,L)$ is an indicator of percolation,

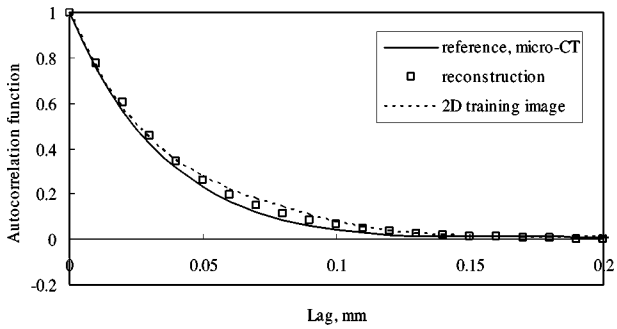

FIG. 13. Void-void autocorrelation functions of Berea sandstone averaged over the three principal orthogonal axes. The autocorrelation function of the reconstructed structure is compared with that of micro-CT (line) and that of a 2D training image (dotted line).

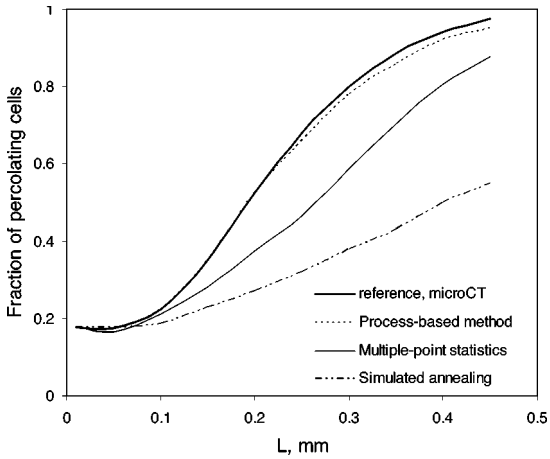

FIG. 14. Fraction of percolating cells for images using different reconstruction methods. Note that incorporating higher-order information in the reconstruction significantly improves the long-range connectivity of the pore space, although it still performs worse than process-based reconstruction methods. The data except multiple-point statistics and micro-CT are taken from [28].

$$\Lambda_3(r,L) = \begin{cases} 1 & \text{if } M(r,L) \text{ percolates 3 directions} \\ 0 & \text{otherwise.} \end{cases} \tag{14}$$

A measurement cube $M(r,L)$ of sidelength L centered at position r is used to calculate the continuous connectedness from one face to opposite face by percolation theory [44]. Twenty-six nearest neighbors in 3D are used to measure the pore connectedness. The reproduction of long-range connectivity by the multiple-point statistics reconstruction for Berea sandstone has already been presented [26]. Here, we briefly repeat the result to show the capability of the method in Fig. 14. The figure also plots the fraction of percolating cells for the reconstruction using simulated annealing and process-based reconstruction [28]. In the figure, the reference measured by micro-CT and the process-based method are similar, but differ from that for the structure generated using simulated annealing. The figure also shows that the reconstruction method based on the low-order correlation functions fail to reproduce the long-range connectivity of porous media, while the process-based method successfully reproduces the connectivity. Our multiple-point statistics method significantly improves the connectivity over the two-point statistics method, although the pore space is still less well connected than the reference image.

G. Permeability by LBM

1. Berea sandstone

For Berea sandstone, as shown in Table I, the computed permeabilities are 1346 mD for the micro-CT image and 1274 mD for the reconstructed microstructure, which are also in good agreement with the experimental value 1100 mD. Here again, the LBM simulation reconfirms the ability to reproduce the long-range connectivity using multiple-point statistics reconstruction although the predicted permeability is still underestimated, which is consistent with the percolation probability shown in Fig. 14.

2. Carbonate rock

Since no microtomographic image of the carbonate rock is available, the LBM simulation is the only way to assess the reconstructed structures. The computed permeability averaged over six realizations after postprocessing is 19.8 mD for the reconstructed microstructures. Although the value is overestimated compared to the experimental permeability of 6.7 mD, the estimation is good considering the significant size difference between the reconstructed images (around 50^3 μm^3) and the experimental plug core that has a volume eight orders-of-magnitude larger. Larger training images can capture more statistics and may produce more realistic images with similar permeability values to the experiment. In addition more information, such as several thin-section images and multi-orientation thin-section images, may improve the results.

VI. CONCLUSIONS

We have proposed a multiple-point statistics method to construct 3D pore-space images from 2D thin sections. The method reproduces typical patterns observed in a training image. We applied the method to Berea sandstone and carbonate samples. We successfully predicted the autocorrelation function, fraction of percolating cells, and permeability computed using the lattice-Boltzmann method (LBM) for Berea.

After validating the method for a sandstone, a carbonate rock was reconstructed and its permeability simulated by the LBM was compared with the experimental value. The predicted permeabilities were overestimated by a factor of three; however, the result is good considering the significant size difference between reconstructed images and the experimental sample.

In this study, a combination of a small 2D image and a 9×9 template with multigrid simulation was sufficient to capture typical patterns seen in the 2D image. However, for more heterogeneous samples more information is needed. The reconstruction can be improved using additional information, such as higher-order information and several thin-section images, including multi-orientation images if the medium is anisotropic, at the expense of more computer power and memory.

ACKNOWLEDGMENTS

The authors would like to express their gratitude to Japan Oil, Gas and Metals National Corporation (JOGMEC) for financial and technical support of our research and to acknowledge JOGMEC for granting permission to publish this paper with the use of the lattice-Boltzmann simulation code. We thank David Stern (ExxonMobil) and Pål-Eric Øren (Statoil) for sharing the experimental data set with us and Peter Lock for providing the code for the effective medium approximation. We also thank the sponsors (BHP, ENI, JOGMEC, Schlumberger, Shell, Statoil, Saudi Aramco, Total, and the U.K. Department of Trade and Industry) of the Imperial College Consortium on Pore-Scale Modelling for financial support.

[1] M. J. Blunt, M. D. Jackson, M. Piri, and P. H. Valvatne, Adv. Water Resour. **25**, 1069 (2002).
[2] S. Chen and G. D. Doolen, Annu. Rev. Fluid Mech. **30**, 329 (1998).
[3] F. A. L. Dullien, *Porous Media: Fluid Transport and Pore Structure* (Academic, San Diego, 1992).
[4] H. Ishida, Annual Report of TRC's activities, Japan National Oil Corporation, 115, 1997.
[5] L. Tomutsa and V. Radmilovic, International Symposium of the Society of Core Analysts, Pau, France, SCA2003-47, 2003.
[6] J. T. Fredrich, Phys. Chem. Earth **24**, 551 (1999).
[7] J. H. Dunsmuir, S. R. Ferguson, K. L. D'Amico, and J. P. Stokes, *Proceedings of SPE Annual Technical Conference and Exhibition, Dallas, 1991*, Paper No. SPE22860.
[8] P. Spanne, J. F. Thovert, C. J. Jacquin, W. B. Lindquist, K. W. Jones, and P. M. Adler, Phys. Rev. Lett. **73**, 2001 (1994).
[9] R. D. Hazlett, Transp. Porous Media **20**, 21 (1995).
[10] S. Bryant and M. J. Blunt, Phys. Rev. A **46**, 2004 (1992).
[11] S. Bakke and P. E. Øren, SPE J. **2**, 136 (1997).
[12] M. Pilotti, Transp. Porous Media **41**, 359 (2000).
[13] F. J. Lucia, *Carbonate Reservoir Characterization* (Springer, Berlin, 1999).
[14] J. A. Quiblier, J. Colloid Interface Sci. **98**, 84 (1984).
[15] P. M. Adler, C. G. Jacquin, and J. A. Quiblier, Int. J. Multiphase Flow **16**, 691 (1990).
[16] P. Levitz, Adv. Colloid Interface Sci. **77**, 71 (1998).
[17] C. L. Y. Yeong and S. Torquato, Phys. Rev. E **57**, 495 (1998).
[18] C. L. Y. Yeong and S. Torquato, Phys. Rev. E **58**, 224 (1998).
[19] M. S. Talukdar, O. Torsaeter, and M. A. Ioannidis, J. Colloid Interface Sci. **248**, 419 (2002).
[20] K. J. Wu, N. Nunan, J. W. Crawford, I. M. Young, and K. Ritz, Soil Sci. Soc. Am. J. **68**, 346 (2004).
[21] J. Yao, P. Frykman, F. Kalaydjian, J. F. Thovert, and P. M. Adler, J. Colloid Interface Sci. **156**, 478 (1993).
[22] B. Biswal, C. Manwart, R. Hilfer, S. Bakke, and P. E. Øren, Physica A **273**, 452 (1999).
[23] C. Manwart, S. Torquato, and R. Hilfer, Phys. Rev. E **62**, 893 (2000).
[24] P. E. Øren and S. Bakke, Transp. Porous Media **46**, 311 (2002).
[25] S. Strebelle, K. Payrazyan, and J. Caers, SPE J. **8**, 227 (2003).
[26] H. Okabe and M. J. Blunt, J. Pet. Sci. Eng. (to be published).
[27] R. D. Hazlett, Math. Geol. **29**, 801 (1997).
[28] P. E. Øren and S. Bakke, J. Pet. Sci. Eng. **39**, 177 (2003).
[29] J. Caers, J. Pet. Sci. Eng. **29**, 177 (2001).
[30] C. V. Deutsch and A. G. Journel, *GSLIB: Geostatistical Software Library and User's Guide*, 2nd ed. (Oxford University Press, Oxford, 1998).
[31] A. G. Journel, Math. Geol. **34**, 573 (2002).
[32] J. Serra, *Image Analysis and Mathematical Morphology* (Aca-

demic, New York, 1992).
[33] P. A. Lock, X. D. Jing, R. W. Zimmerman, and E. M. Schlueter, J. Appl. Phys. **92**, 6311 (2002).
[34] J. J. Buckles, R. D. Hazlett, S. Y. Chen, K. G. Eggert, and W. E. Soll, Los Alamos Sci. **22**, 112 (1994).
[35] F. M. Auzerais, J. Dunsmuir, B. B. Ferreol, N. Martys, J. Olson, T. S. Ramakrishnan, D. H. Rothman, and L. M. Schwartz, Geophys. Res. Lett. **23**, 705 (1996).
[36] D. Grunau, S. Y. Chen, and K. Eggert, Phys. Fluids A **5**, 2557 (1993).
[37] Japan National Oil Corporation's report, 2003.
[38] P. L. Bhatnagar, E. P. Gross, and M. Krook, Phys. Rev. **94**, 511 (1954).
[39] S. Wolfram, J. Stat. Phys. **45**, 471 (1986).
[40] B. Ferreol and D. H. Rothman, Transp. Porous Media **20**, 3 (1995).
[41] C. Manwart, U. Aaltosalmi, A. Koponen, R. Hilfer, and J. Timonen, Phys. Rev. E **66**, 016702 (2002).
[42] T. Oshita and H. Okabe, International Symposium of the Society of Core Analysts, Abu Dhabi, UAE, SCA2000-08, 2000.
[43] R. Hilfer, Transp. Porous Media **46**, 373 (2002).
[44] D. Stauffer and A. Aharnony, *Introduction to Percolation Theory*, revised 2nd ed. (Taylor & Francis, London, 1994).